nature chemistry

ARTICLES

https://doi.org/10.1038/s41557-022-00925-0

Check for updates

Stabilization of hexazine rings in potassium polynitride at high pressure

Yu Wang[1], Maxim Bykov[2,3], Ilya Chepkasov[4], Artem Samtsevich[4], Elena Bykova[2], Xiao Zhang[1], Shu-qing Jiang[1], Eran Greenberg[5,6], Stella Chariton[5], Vitali B. Prakapenka[5], Artem R. Oganov[4] and Alexander F. Goncharov[2]✉

Polynitrogen molecules are attractive for high-energy-density materials due to energy stored in nitrogen–nitrogen bonds; however, it remains challenging to find energy-efficient synthetic routes and stabilization mechanisms for these compounds. Direct synthesis from molecular dinitrogen requires overcoming large activation barriers and the reaction products are prone to inherent inhomogeneity. Here we report the synthesis of planar N_6^{2-} hexazine dianions, stabilized in K_2N_6, from potassium azide (KN_3) on laser heating in a diamond anvil cell at pressures above 45 GPa. The resulting K_2N_6, which exhibits a metallic lustre, remains metastable down to 20 GPa. Synchrotron X-ray diffraction and Raman spectroscopy were used to identify this material, through good agreement with the theoretically predicted structural, vibrational and electronic properties for K_2N_6. The N_6^{2-} rings characterized here are likely to be present in other high-energy-density materials stabilized by pressure. Under 30 GPa, an unusual $N_2^{0.75-}$-containing compound with the formula $K_3(N_2)_4$ was formed instead.

Nitrogen-rich compounds are widely investigated as high-energy-density materials (HEDM)[1,2]. Their substantial energy storage or release capacity (up to 2.3 eV per atom) is related to the large energy difference of the single/double versus the triple bonds between nitrogen atoms. Numerous all-nitrogen species were predicted theoretically[3–7]; however, only a few such species have hitherto been reported[1,8,9]. One major obstacle is the low-order N–N bonds tend to be unstable at low pressures. They can be stabilized under pressure, however, providing a pathway for synthesis. At about 50 GPa, molecular diatomic nitrogen has been theoretically predicted to transform into an atomic solid with a single-bonded crystalline cubic gauche (cg-N) structure[6], which was later experimentally demonstrated in the laser-heated diamond anvil cell (DAC) at 110 GPa and 2500 K (ref. [10]). The high pressures required for formation of polynitrogens, however, as well as the difficulties in recovering these species under ambient (or practical) conditions, make this synthetic route challenging.

Theoretical calculations have previously predicted a number of high-pressure nitrogen-rich compounds with metals that form unusually few-bonded all-nitrogen groups as well as polymeric networks[11–21]. Stabilization of polynitrogen groups at ambient pressure commonly occurs in very complex compounds at the expense of the energy density yield[22–26]. Great progress has recently been made in synthesis and stabilization of various pentazolate anion cyclo-N_5^- compounds[27–30]; however, their stability in common environments and energy yields still remain a matter of investigation. Application of pressure may allow stabilization of various nitrogen species in simple compounds with metals. A variety of compounds containing polymeric nitrogen chains were synthesized in several metal–nitrogen systems (for example, Be, Mg, Ta, Fe) at pressures between 50 and 100 GPa (refs. [31–34]). BeN_4 and Mg_2N_4 were found to be recoverable at atmospheric pressure, which suggests novel opportunities with regard to synthesis of HEDMs. Even more complex nitrogen rich compounds such as porous frameworks with transition metals (Re, Hf, W and Os), where the structure combines nitrogen low-order bonded chains and triply bonded nitrogen molecules have been synthesized above 100 GPa (refs. [18,35,36]). A WN_6 compound with a single-bonded N_6 in a chair conformation ring has recently been synthesized above 126 GPa by laser heating tungsten in an N_2 environment[37].

Alkali metal–nitrogen compounds were proposed to reduce the pressure of synthesis and to improve the compound stability and energy density of HEDMs as they are predicted to form a wealth of materials with various structures and compositions at high pressures[38–52]. The structural motifs include penta-N_5^- salts, N_6^{2-} hexazine dianions and polymeric chains, and some of them are predicted to be preserved at ambient conditions. Yet there are only a few experimental reports that support these findings. Steele et al. synthesized a penta-N_5^- salt of caesium[45] by laser heating CsN_3 azide in molecular N_2 medium at 60 GPa in a DAC. The crystal structure of this CsN_5 compound with six formula units in the unit cell is very complex and it was determined by comparing powder X-ray diffraction (XRD) and Raman spectroscopy results with theoretical calculations. Laniel and colleagues synthesized an LiN_5 compound with penta-N_5^- ions by heating lithium in N_2 medium at 45 GPa, but the precise atomic configuration could not be resolved due to powder nature of the sample[53,54]. They also documented the synthesis of lithium diazenide LiN_2 at lower pressures. In a more recent work, Bykov and colleagues[55] synthesized two pentazolate (Na_2N_5 and NaN_5) and two diazenide ($Na_3(N_2)_4$ and NaN_2) structures at ~50, 28 and 4 GPa by laser heating sodium azide NaN_3. Use of azides containing linear N_3^- groups as precursors allows to reduce substantially (for example, compared with molecular N_2) the activation barrier for the reaction and provide more uniform reaction

[1]Key Laboratory of Materials Physics, Institute of Solid State Physics, HFIPS, Chinese Academy of Sciences, Hefei, China. [2]Earth and Planets Laboratory, Carnegie Institution of Washington, Washington, DC, USA. [3]Department of Mathematics, Howard University, Washington, DC, USA. [4]Skolkovo Institute of Science and Technology, Skolkovo Innovation Center, Moscow, Russia. [5]Center for Advanced Radiations Sources, University of Chicago, Chicago, IL, USA. [6]Present address: Applied Physics Division SNRC, Yavne, Israel. ✉e-mail: agoncharov@carnegiescience.edu

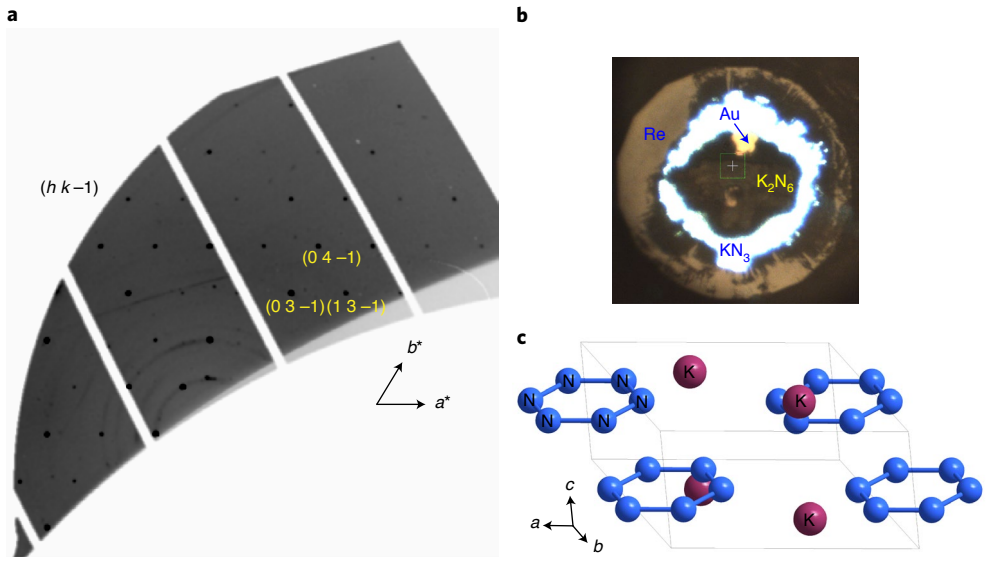

Fig. 1 | Single-crystal X-ray diffraction data in compressed to 50 GPa and laser heated via direct coupling KN_3 without a pressure medium. a, A part of the reconstructed (*h k* –1) precession image from the single-crystal XRD dataset of K_2N_6 at ~50 GPa, demonstrating the crystal quality and the diffraction selection rules. The details of structural refinement are presented in Supplementary Table 2. **b**, A microphotograph of the sample in transmitted and reflected light at 50 GPa, which is transformed in the central more reflecting part. **c**, The crystal structure of K_2N_6 at ~50 GPa.

environment. Polymerization of various azides has been widely investigated in static DAC experiments[56,57], mainly at room temperature, and theoretically. The experiments show a rich polymorphism at high pressures, but the azide group remains (meta)stable[57–60] up to at least 60 GPa (in lithium azide); however, Raman spectroscopy in NaN_3 azide above 19 GPa shows[56] an appearance of additional Raman bands at 1800–2000 cm^{-1}, which cannot be explained by the azide groups and probably indicate a chemical transformation as no associated phase transformation has been detected. It is interesting that the Raman bands in this spectral range can be also observed after a photochemical transformation at much lower pressures (4.8–8.1 GPa); however, no XRD signature of the transformation could be found[61]. Here we report a synthesis from KN_3 of a previously predicted K_2N_6 compound at about 50 GPa; this compound features planar hexazine dianions N_6^{2-}.

Results

The synchrotron XRD and Raman experiments in DAC are described in the Methods. In this work we focus on the experiments in which powdered potassium azide (KN_3) was investigated without any pressure medium/reagent, which gives preference to the formation of compounds with this composition. Further experiments in which molecular N_2 was loaded together with KN_3 are used to investigate the room-temperature compression and low-temperature decompression behaviour via in situ Raman measurements. First-principles theoretical calculations (see Methods) have been performed on the previously predicted *I*4/*mcm*, *C*2/*m* and *P*6/*mmm* KN_3 structures[44,47], and also explored the transition pathways between them.

It was previously shown that when compressed at room temperature, KN_3 experiences phase transformations from *I*4/*mcm* to another structure at about 15 GPa (refs. [59,60]), which is predicted by theoretical calculations[44,47] to be *C*2/*m*. In this phase the linear N_3 azide groups are aligned parallel to each other unlike the low-pressure *I*4/*mcm*, where they are alternately rotated by 90° with respect to each other. Our Raman spectroscopy data (Supplementary Fig. 1) do show a transformation above 15 GPa that is manifested by the splitting of the librational modes and appearance of new peaks, in good agreement with ref. [59]. Above 30 GPa, the Raman spectra show a broad band near 1900 cm^{-1} that increases in intensity with pressure, similar to that reported previously in NaN_3 (ref. [56]). Our XRD data at ~50 GPa—which generally agree with the extrapolated results of ref. [60]—reveal a poorly crystallized single crystal of KN_3 with extremely broad diffracted peaks (Supplementary Fig. 2). The unconstrained lattice determination results in the following unit-cell parameters $a = 5.4252(13)$, $b = 5.487(11)$, $c = 4.67(4)$ Å; $\alpha = 90.6(4)°$, $\beta = 92.2(4)°$, $\gamma = 90.22(17)°$. This indexing suggests that this phase is just a heavily distorted *I*4/*mcm* ambient pressure structure. The refinement against single-crystal data using the undistorted *I*4/*mcm* model results in an R_1 factor of ~11%, which clearly indicates that no major structural rearrangements take place, thus ruling out the predicted *C*2/*m* phase. The best refinement was obtained in a monoclinic space group *I*2/*c* (Supplementary Fig. 3 and Supplementary Table 1).

It is worth noting that KN_3 is sensitive to X-ray exposure, as evidenced by a darkening of the sample (Fig. 1b), a distinct Raman spectrum (Fig. 2), and time-dependent XRD patterns (Supplementary Fig. 4). The irradiated product demonstrates a substantial reduction in intensity of the N_3 azide Raman modes and sharpening and strengthening of the Raman peaks, which could be assigned to yet unidentified definitely polynitrogen configuration; however, time-dependent X-ray diffraction measurements do not show the appearance of new diffracted peaks, suggesting that the X-ray-induced phase is amorphous in nature (Supplementary Fig. 4).

The theoretically predicted phase transformations to another azide polymorph *C*2/*m* KN_3 and hexazine *P*6/*mmm* K_2N_6 (refs. [42,44,47,52]) are reconstructive (which involves large rearrangements of the atoms and chemical bonds) and thus are kinetically hindered (impeded and delayed) due to the high kinetic barriers. The transformation barriers theoretically calculated in this work are high: 137 meV per atom for the transition from *I*4/*mcm* to *C*2/*m* KN_3 at 30 GPa, and 426 meV per atom from *I*4/*mcm* to *P*6/*mmm* at 50 GPa (Supplementary Figs. 5 and 6). We performed high-temperature treatment of cold-compressed KN_3 to overcome these barriers. At 49–53 GPa, laser heating of KN_3 to 2500 K results in the formation of a new material that is clearly identified by shiny surfaces and a very distinct XRD pattern (Fig. 1 and Supplementary Fig. 7). The new phase was obtained in the form of fine-grain powder, as well

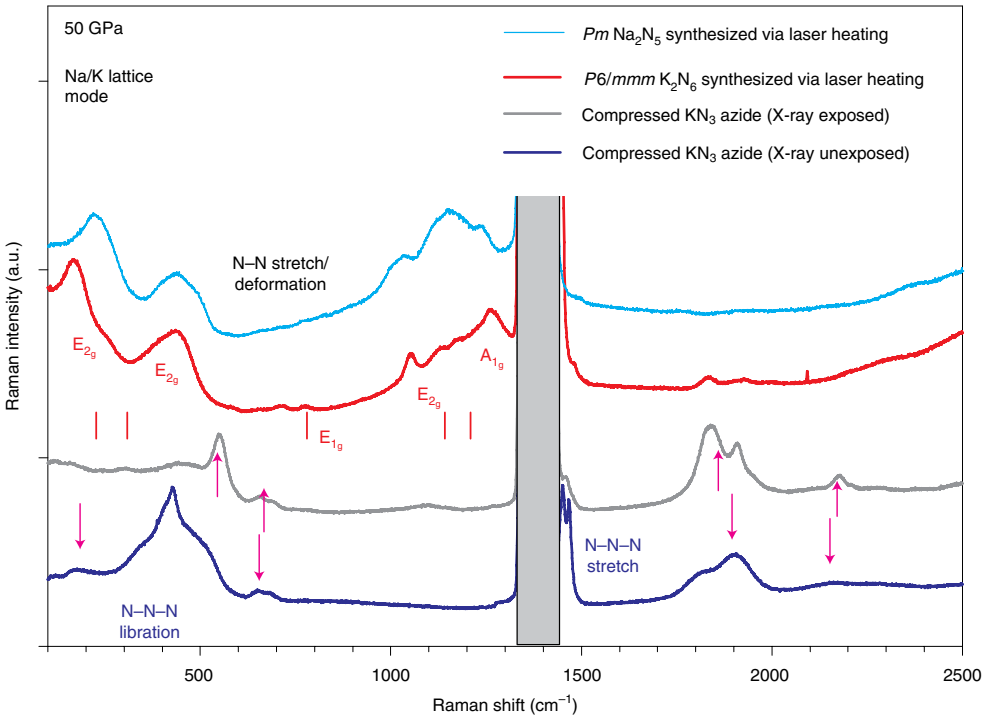

Fig. 2 | Raman spectra of X-ray-unexposed and -exposed KN_3 before and after laser heating at around 50 GPa. The pink arrows show the Raman peaks that emerge under pressure due to X-ray radiation, which are assigned to yet-unidentified polynitrogen species. The ticks show the theoretically calculated positions of the Raman modes of *P6/mmm* K_2N_6. Observed *P6/mmm* K_2N_6 Raman peaks are labelled according to the mode assignment based on comparison with theory. Structurally similar *Pm* Na_2N_5 Raman spectra[55] are shown for comparison, supporting these assignments. The shaded area indicates the spectral ranges, where Raman peaks of the stressed diamond anvils appear. a.u., arbitrary units.

as in the form of single crystals. The unit cell was indexed with a hexagonal unit cell ($a=5.2855(9)$, $c=2.6186(5)$ Å for the powder sample; and $a=5.281(3)$, $c=2.661(2)$ Å for the single crystals; see Fig. 1, Supplementary Fig. 7 and Supplementary Tables 2 and 3). This lattice is in a good agreement with the predicted high-pressure polymorphs of KN_3–K_2N_6 with *P6/mmm* symmetry[44,47,52]. Indeed, structure refinement against single-crystal diffraction dataset based on this model converges with excellent agreement factors (Supplementary Table 2). In the *P6/mmm* structure, potassium and nitrogen atoms occupy Wyckoff sites 2*c* (1/3, 2/3, 0) and 6*k* (0.776(3), 0, 0.5), respectively (Supplementary Table 2). Nitrogen atoms are connected with each other, forming planar N_6 rings (Fig. 1c), whereas potassium atoms are twelve-coordinated by nearby nitrogen atoms, forming truncated triangular prisms. The refined N–N bond length of 1.184(13) Å is somewhat shorter than the theoretical predictions[44,47,52]. We should note that the high-symmetry hexagonal structure may also come as a result of rotational disorder of N_5 groups, such as in the high-temperature form of sodium pentazolate Na_2N_5 (ref. [55]); however, electron density peaks corresponding to the positions of nitrogen atoms in the potassium-bearing compound studied here form a clearly hexagonal ring pattern even if the structure is refined in lower symmetry (we have tested subgroups *P6/m*, *Cmmm*, *Pm*, *P2*, *C2/m*, *Cm* and *P1* with relevant twinning options). The theoretical unit cell parameters slightly differ (*a* is 5% larger, whereas *c* is 6% smaller) from the experimentally determined ones yielding the volume discrepancy within fair 4% (Fig. 3). The experiments show that *P6/mmm* phase can be synthesized up to at least 99 GPa and it remains stable up to 128 GPa. On the other hand, *P6/mmm* phase synthesized at 50–60 GPa has been found to remain metastable down to 21 GPa on unloading at 80 and 297 K (Fig. 3 and Supplementary Fig. 8). The compressional behaviour is in fair agreement with theoretical calculations[44,47] (Fig. 3).

Considering the oxidation state of potassium is +1, each N_6 ring must accommodate two electrons leading to an eight-π-electron system in N_6^{2-}. This system is therefore antiaromatic, with two extra electrons entering partially filled π^* orbitals, leading to metallic character of this compound, in agreement with theoretical calculations of the electronic band structure (Supplementary Fig. 9). The intramolecular bond in the hexazine dianions ring is probably resonant; the bond order 1.33 can be calculated on the basis of the charge transfer of two electrons from potassium to the N_6 rings. Theoretical calculations[44,47,52] predicted that *P6/mmm* KN_3 would be a stable polymorph above 40–50 GPa, which is mostly consistent with our observations.

The Raman spectra measured concomitantly with XRD change drastically following the transformation (Fig. 2), where all of the X-ray-exposed and -unexposed azide peaks disappear and thus all of the observed Raman peaks correspond to a pure N_6^{2-} hexazine dianion K_2N_6 compound. The *P6/mmm* KN_3 synthesized in this work shows distinctive Raman bands in the spectral range characteristic for the stretching vibrations of a few-bonded nitrogen (1000–1300 cm^{-1}), and two low-frequency modes in the spectral range of the N–N bending modes and lattice vibrations. Weak peaks at ~700 cm^{-1} can also be seen. We have been able to trace the Raman spectrum of this phase down to approximately 20 GPa on unloading (Supplementary Fig. 8), thus establishing their pressure behaviour and allowing comparison with theoretical calculations[44] of vibrational frequencies of *P6/mmm* KN_3 at 100 GPa (Fig. 4) and a hypothetic N_6 hexaazabenzene molecule, where the ring is out-of-plane distorted with the D_2 symmetry[7]. These data provide very important clues for assigning the observed Raman modes of synthesized here *P6/mmm* KN_3 (Fig. 4). Moreover, we have performed first-principles calculations of the vibrational and electronic properties of *P6/mmm* K_2N_6 and *Pm* K_2N_5 (ref. [55];

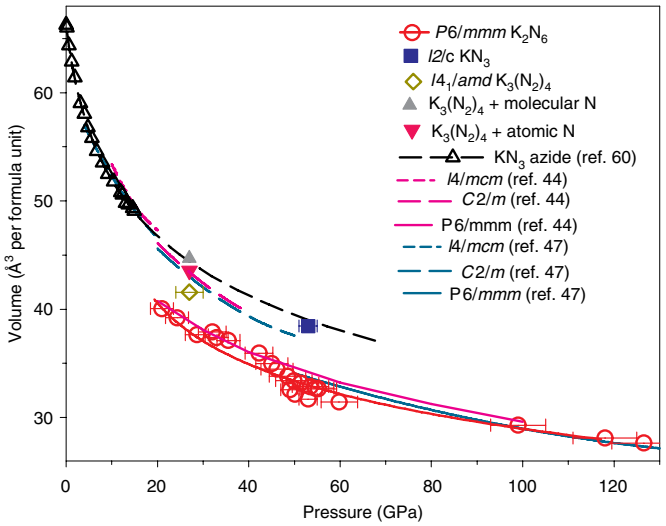

Fig. 3 | Volumes per formula unit of K–N compounds investigated here. KN_3 azide—the *I4/mcm* structure of which was determined up to 15 GPa (ref. [60])—develops a monoclinic distortion with the space group *I2/c* (determined at 53 GPa; Supplementary Figs. 2 and 3, and Supplementary Table 1) where it transforms on laser heating into a *P6/mmm* K_2N_6 compound with N_6^{2-} hexazine dianions, which is some 17% denser. However, *I4₁/amd* $K_3(N_2)_4$ diazenide (synthesized at 30 GPa, also assisted by laser heating), which is slightly deficient in nitrogen, has about the same density as *I2/c* azide. To take into account the difference in composition we added a volume of nitrogen in molecular and monatomic (cg-N) compounds at the same pressure determined from their equations of states[64,65]. The theoretical volumes of *I4/mcm* and *C2/m* (which we do not observe) KN_3, and *P6/mmm* K_2N_6, are shown for comparison[44,47].

Methods), which allow the direct comparison of the experimental and theoretical Raman mode frequencies at 50 GPa.

The group theory predicts four $A_{1g}+2E_{2g}+E_{1g}$ Raman-active modes for the N_6^{2-} rings and one E_{2g} mode for potassium vibrations of *P6/mmm* K_2N_6; no translation or rotation modes are expected from the N_6^{2-} rings as there is only one ring in the unit cell. The lowest-frequency mode corresponds to E_{2g} vibrations of potassium atoms in the *xy* plane. This assignment is supported by the fact that a similar mode of *Pm* Na_2N_5 (ref. [55]), which is analogous to *P6/mmm* K_2N_6 in the crystal structure, has a distinctly higher frequency (Fig. 2). The strong mode at approximately 400 cm^{-1} is assigned to the E_{2g} in-plane deformation mode, whereas the weak peak at 750 cm^{-1}—to the E_{1g} out-of-plane deformation mode of the hexazine ring. This assignment is based on the frequency sequence of the deformation bands calculated in ref. [7] (correlated in symmetry to those of the symmetric D_{6h} planar ring) and our Raman calculations; we also assumed that the E_{2g} in-plane deformation mode must be stronger as it modulates intra-ring N–N bonds while the E_{1g} out-of-plane mode is purely deformational. The two other in-plane vibrations at higher frequencies also yield strong Raman bands corresponding to the E_{2g} in-plane mixed stretching deformation mode and the symmetric breathing A_{1g} stretching mode; the latter is expected to be the dominant Raman band (Fig. 2). There are weaker Raman peaks between these modes at ~1150 cm^{-1} (Supplementary Fig. 10) and also a band at 700 cm^{-1}, which cannot be assigned to any Raman-active fundamental vibrations when assuming the D_{6h} symmetry of the planar N_6^{2-} ring; however, the other stretching deformation modes (which are nominally infrared active) can contribute to Raman processes in the case of symmetry reduction (such as dynamical)—for example, to the non-planar twist-boat D_2 structure[7], even though our single-crystal XRD data show a planar ring structure. Note that K_2N_6 is a metal and so the overall peak broadening can be assigned to the coupling with the carriers. The frequencies of the characteristic N–N stretching deformation modes decrease with pressure release and these dependencies extrapolate reasonably well to the theoretically calculated values of the twist-boat N_6 isomer at ambient pressure[7]. Note that the frequencies and the pressure dependencies of the fundamental modes of the N_6^{2-} ring are close to those of pentazolate rings measured previously[45,53] in CsN_5 and LiN_5 (Supplementary Fig. 11). Moreover, the calculated here Raman modes of *Pm* K_2N_5 with pentazolate rings are also close in frequency (Fig. 4), albeit the number of predicted Raman modes is much larger than observed (Fig. 4). Nonetheless, the Raman spectra of *P6/mmm* K_2N_6 and *Pm* Na_2N_5 are clearly distinct in the spectral range of the fundamental modes of the nitrogen rings (Fig. 2), especially for the stretching-deformation modes at 1100–1300 cm^{-1}, supporting the presence of N_6^{2-} rings in *P6/mmm* K_2N_6.

On unloading of *P6/mmm* K_2N_6 at room temperature, we find that the structure is preserved down to 21 GPa and no X-ray decomposition was detected. On unloading at 78 K, the Raman spectra show clear signs of deterioration of this compound at 22 GPa, where the characteristic bands become weaker and other broad bands at 400, 1800, 2100 and 2300 cm^{-1} increase in intensity (Supplementary Fig. 8). The product is difficult to identify; it is definitely not azide as there is no sign of the characteristic N–N stretching mode of the linear N_3 groups. Based on observations of a number of high-frequency modes this product is probably a highly disordered state with elongated N_2 molecules. The Raman spectrum of this material is qualitatively similar to that of the cold compressed azide (Fig. 2).

Laser heating to 2500 K of laser- and X-ray-unexposed KN_3 azide, first pressurized to 50 GPa and then unloaded at room temperature to 30 GPa, results in the formation of a shiny material that looks similar to K_2N_6 but is different in structure and composition judging from single-crystal XRD and Raman spectroscopy measurements (Fig. 5). Similar results were obtained in the loading cycle probed by Raman. The reaction products tend to be textured and

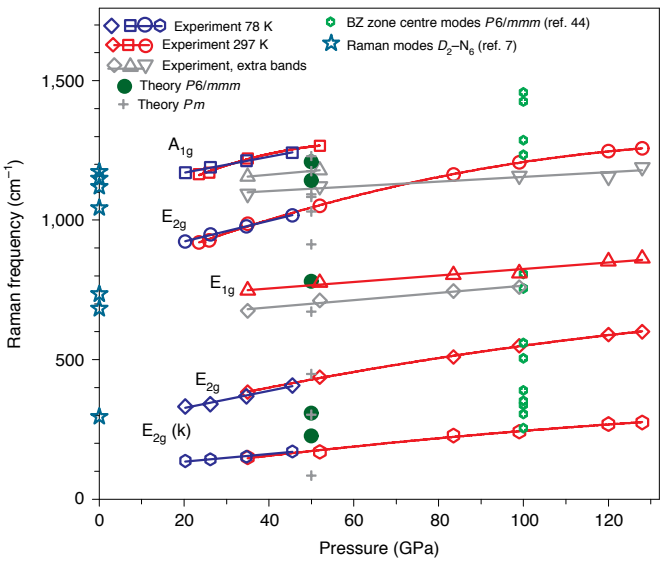

Fig. 4 | Vibrational frequencies of *P6/mmm* K_2N_6. The results deduced from the Raman spectra are compared with the theoretically calculated Raman frequencies for *P6/mmm* K_2N_6 and *Pm* K_2N_5, Brillouin zone centre vibrational modes of *P6/mmm* K_2N_6 (ref. [44]) and the Raman-active modes of a N_6 ring isomer in the twist-boat D_2 structure[7]. The error bars for the Raman frequencies are smaller than the symbol size. Above 80 GPa, the A_{1g} mode cannot be observed as it interferes with the Raman signal from diamond anvils. These results support the presented here vibrational modes assignment of *P6/mmm* K_2N_6.

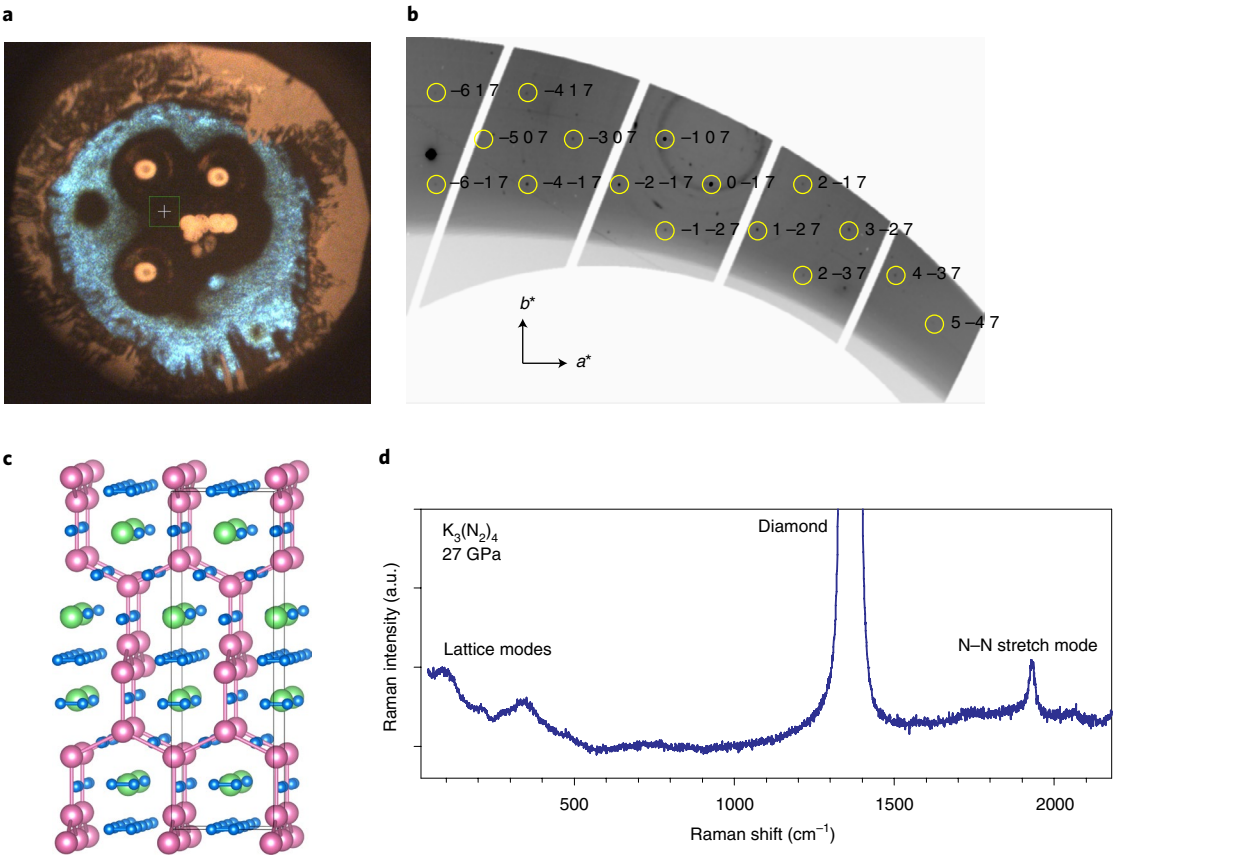

Fig. 5 | Experimental data on $I4_1/amd$ $K_3(N_2)_4$ synthesized at 30 GPa by laser heating of KN_3. a, A microphotograph of a KN_3 sample laser heated in several places, revealing shiny areas where a new material is synthesized. Transparent parts of the sample (unexposed KN_3 azide) appear light blue in the transmitted light. **b**, A part of the reconstructed (*h k* 7) precession image from the single-crystal XRD dataset of $K_3(N_2)_4$ at ~27 GPa. Reflections *hkl* with $h+k+l=2n+1$ are absent due to the *I*-centring of the lattice. **c**, The structure of $I4_1/amd$ $K_3(N_2)_4$, which consists of two potassium sublattices (pink and green spheres) and two elongated N_2 sublattices (blue spheres). **d**, The Raman spectra of $K_3(N_2)_4$ at ~27 GPa. A high-frequency band corresponds to the N–N stretching mode of dinitrogen. The low-frequency modes are vibrations of potassium atoms and lattice vibrations of dinitrogens.

single crystals of good quality and sufficient sizes can be selected by mapping the heated sample area. This material is stable to X-ray irradiation, unlike the initial KN_3 azide. The structure and composition of the synthesized material were directly solved to be $I4_1/amd$ $K_3(N_2)_4$ (which is isostructural with $Na_3(N_2)_4$; Supplementary Table 4). This material has been synthesized in similar P–T conditions in our previous work[62].

Discussion

Past experiments on various azides at high pressures showed the stability of the linear N_3^- ion to at least 60 GPa, judging from vibrational spectroscopy[56–60,63]. Theoretical calculations predict a major phase transformation within this chemical structure to a monoclinic $C2/m$, where the linear N_3^- groups become collinear on forming the $C2/m$ structure[44,47]. LiN_3 at ambient pressure and α-NaN_3 at 0.3–17 GPa have the same structure[46,58]. However, our experiments show that this transformation does not occur in potassium azide up to at least 50 GPa. At room temperature, KN_3 is reported to transform under pressure to another phase with linear N_3^- groups[59,60], but the structure of this phase is not monoclinic $C2/m$. Instead our data (Supplementary Figs. 2–4) show that it prefers to remain in an only slightly distorted $I4/mcm$ structure, preserving the original lattice to at least 50 GPa; however, the azide ion becomes chemically unstable in this regime as manifested by formation of other yet-unidentified polynitrogen species above 30 GPa (as evidenced via emergence of a 1900 cm^{-1} Raman band; Supplementary Fig. 1) a process that is accelerated by X-ray radiation exposure.

These results show that the azide ion N_3^- configuration becomes unstable at high pressures. Our high-pressure laser heating experiments revealed two new classes of compounds that become stable at these conditions. The structural and vibrational spectroscopy data provide concerted consistent data identifying their physical and chemical structure.

The N_6^{2-} hexazine dianion ring compound discovered here represents a previously unobserved polynitrogen configuration with low-order nitrogen–nitrogen bonds. The energy yield for this prototypic material can be estimated from the enthalpy versus pressure curves[44,47,52] extrapolated to ambient pressure. This yields about 160 kJ mol^{-1} (1.7 eV), which is comparable to that of a common explosive. Although this material cannot be recovered to ambient pressure, we hope that this study will help with the search and synthesis of other polynitrogens, which are potentially energetic and recoverable.

Laser heating of KN_3 azide at 30 GPa results in the formation of an unexpected diazenide $I4_1/amd$ $K_3(N_2)_4$ with a complex structure, which contains potassium atoms and elongated $N_2^{0.75-}$ anions with different site symmetries, and a very large unit cell. The theoretically predicted $C2/m$ azide polymorph is not obtained even though the transformation barrier (Supplementary Fig. 5) is not very high and can definitely be overcome with laser heating assistance. It is interesting that the diazenide structure does not seem to reveal more efficient packing than azide as the specific volume of $K_3(N_2)_4$ is very similar to that of KN_3 azide (Fig. 3). It is likely that synthesis of this structure is at least partially due to its high entropy

stemming from rotating dinitrogens. By contrast, the formation of K_2N_6 with hexazine dianions rings at 50 GPa is accompanied by a large volume contraction (about 17%), which explains the importance of pressure in its synthesis. This transformation leads to the formation of few-bonded polynitrogen species, at relatively low pressure compared to monatomic polymeric nitrogen.

Varying the reagent compositions during the synthesis (for example, by providing an excess of nitrogen) would lead to the formation of compounds other than the ones explored here. Our preliminary experiments suggest that laser heating of KN_3 in N_2 results in a wealth of new compounds, including various polynitrogen species, with different compositions and structures; these results will be presented in detail elsewhere.

Conclusions

Our experiments show that the azide group N_3^- is prone to chemical destabilization under pressure, as evidenced by a loss of crystallinity of the compressed sample at 300 K, spontaneous emergence of extra Raman bands, and sensitivity to X-ray radiation. The reaction products likely comprise modified variety of nitrogen species such as, for example, dinitrogen-containing compounds and/or square plane D_{2h} N_4^+ (ref. [56]); however, the lack of crystallinity hinders their identification. Depending on the pressure of the synthesis, two new crystalline materials form following laser heating: hexazine dianions ring stabilized in K_2N_6 above 45 GPa, which remains metastable down to 20 GPa, and an unusual $K_3(N_2)_4$ diazenide at 30 GPa. Neither compound, however, was stable under ambient conditions. The high-pressure synthesis of polynitrogen compounds from azides may be scalable, and may promote the formation of various polynitrogen species with different compositions and structures.

Online content

Any methods, additional references, Nature Research reporting summaries, source data, extended data, supplementary information, acknowledgements, peer review information; details of author contributions and competing interests; and statements of data and code availability are available at https://doi.org/10.1038/s41557-022-00925-0.

Received: 2 September 2020; Accepted: 8 March 2022;
Published online: 21 April 2022

References

1. Christe, K. O., Wilson, W. W., Sheehy, J. A. & Boatz, J. A. N_5^+: a novel homoleptic polynitrogen ion as a high energy density material. *Angew. Chem. Int. Ed.* **38**, 2004–2009 (1999).
2. Lauderdale, W. J., Stanton, J. F. & Bartlett, R. J. Stability and energetics of metastable molecules: tetraazatetrahedrane (N_4), hexaazabenzene (N_6), and octaazacubane (N_8). *J. Phys. Chem.* **96**, 1173–1178 (1992).
3. Glukhovtsev, M. N., Jiao, H. & Schleyer, P. V. R. Besides N_2, what is the most stable molecule composed only of nitrogen atoms? *Inorganic Chemistry* **35**, 7124–7133 (1996).
4. Hirshberg, B., Gerber, R. B. & Krylov, A. I. Calculations predict a stable molecular crystal of N_8. *Nat Chem* **6**, 52–56 (2014).
5. Zahariev, F., Hooper, J., Alavi, S., Zhang, F. & Woo, T. K. Low-pressure metastable phase of single-bonded polymeric nitrogen from a helical structure motif and first-principles calculations. *Phys. Rev. B* **75**, 140101 (2007).
6. Mailhiot, C., Yang, L. H. & McMahan, A. K. Polymeric nitrogen. *Phys. Rev. B* **46**, 14419 (1992).
7. Tobita, M. & Bartlett, R. J. Structure and stability of N_6 isomers and their spectroscopic characteristics. *J. Phys. Chem. A* **105**, 4107–4113 (2001).
8. Samartzis, P. C. & Wodtke, A. M. All-nitrogen chemistry: how far are we from N_{60}? *Int. Rev. Phys. Chem.* **25**, 527 (2006).
9. Samartzis, P. C. & Wodtke, A. M. Casting a new light on azide photochemistry: photolytic production of cyclic-N_3. *Phys. Chem. Chem. Phys.* **9**, 3054–3066 (2007).
10. Eremets, M. I., Gavriliuk, A. G., Trojan, I. A., Dzivenko, D. A. & Boehler, R. Single-bonded cubic form of nitrogen. *Nat. Mater.* **3**, 558–563 (2004).
11. Wilson, K. J., Perera, S. A., Bartlett, R. J. & Watts, J. D. Stabilization of the pseudo-benzene N_6 ring with oxygen. *J. Phys. Chem. A* **105**, 7693–7699 (2001).
12. Wang, W. et al. High-pressure bonding mechanism of selenium nitrides. *Inorganic Chemistry* **58**, 2397–2402 (2019).
13. Zhang, S., Zhao, Z., Liu, L. & Yang, G. Pressure-induced stable BeN_4 as a high-energy density material. *J. Power Sources* **365**, 155–1161 (2017).
14. Liu, Z. et al. Nitrogen-rich GaN_5 and GaN_6 as high energy density materials with modest synthesis condition. *Phys. Lett. A* **383**, 125859 (2019).
15. Li, J., Sun, L., Wang, X., Zhu, H. & Miao, M. Simple route to metal *cyclo*-N_5^- salt: high-pressure synthesis of CuN_5. *J. Phys. Chem. C* **122**, 22339–22344 (2018).
16. Zhang, Y. et al. Diverse ruthenium nitrides stabilized under pressure: a theoretical prediction. *Sci. Rep.* **6**, 33506 (2016).
17. Straka, M. N_6 ring as a planar hexagonal ligand in novel M(η^6-N_6) species. *Chem. Phys. Lett.* **358**, 531–536 (2002).
18. Zhang, J., Oganov, A. R., Li, X. & Niu, H. Pressure-stabilized hafnium nitrides and their properties. *Phys. Rev. B* **95**, 020103 (2017).
19. Kvashnin, A. G., Oganov, A. R., Samtsevich, A. I. & Allahyari, Z. Computational Search for novel hard chromium-based materials. *J. Phys. Chem. Lett.* **8**, 755–764 (2017).
20. Yu, S. et al. Emergence of novel polynitrogen molecule-like species, covalent chains, and layers in magnesium–nitrogen Mg_xN_y phases under high pressure. *J. Phys. Chem. C* **121**, 11037–11046 (2017).
21. Huang, B. & Frapper, G. Barium–nitrogen phases under pressure: emergence of structural diversity and nitrogen-rich compounds. *Chem. Mater.* **30**, 7623–7636 (2018).
22. Zhang, C., Sun, C., Hu, B., Yu, C. & Lu, M. Synthesis and characterization of the pentazolate anion *cyclo*-N_5^- in $(N_5)_6(H_3O)_3(NH_4)_4Cl$. *Science* **355**, 374–376 (2017).
23. Xu, Y. et al. A series of energetic metal pentazolate hydrates. *Nature* **549**, 78 (2017).
24. Xu, Y., Lin, Q., Wang, P. & Lu, M. Syntheses, crystal structures and properties of a series of 3D metal–inorganic frameworks containing pentazolate anion. *Chem. Asian J.* **13**, 1669–1673 (2018).
25. Sun, C. et al. Synthesis of AgN_5 and its extended 3D energetic framework. *Nat. Commun.* **9**, 1269 (2018).
26. Zhang, W. et al. Stabilization of the pentazolate anion in a zeolitic architecture with $Na_{20}N_{60}$ and $Na_{24}N_{60}$ nanocages. *Angew. Chem. Int. Ed.* **57**, 2592–2595 (2018).
27. Yao, Y., Lin, Q., Zhou, X. & Lu, M. Recent research on the synthesis pentazolate anion cyclo-N_5^-. *FirePhysChem* **1**, 33–45 (2021).
28. Christe, K. O. Polynitrogen chemistry enters the ring. *Science* **355**, 351–351 (2017).
29. Wozniak, D. R. & Piercey, D. G. Review of the current synthesis and properties of energetic pentazolate and derivatives thereof. *Engineering* **6**, 981–991 (2020).
30. Ren, G. et al. Theoretical perspective on the reaction mechanism from arylpentazenes to arylpentazoles: new insights into the enhancement of cyclo-N_5 production. *Chem. Commun.* **55**, 2628–2631 (2019).
31. Bykov, M. et al. Fe-N system at high pressure reveals a compound featuring polymeric nitrogen chains. *Nat Commun* **9**, 2756 (2018).
32. Laniel, D. et al. Synthesis of magnesium-nitrogen salts of polynitrogen anions. *Nat. Commun.* **10**, 7 (2019).
33. Bykov, M. et al. High-pressure synthesis of Dirac materials: layered van der Waals bonded BeN_4 polymorph. *Phys. Rev. Lett.* **126**, 175501 (2021).
34. Bykov, M. et al. Stabilization of polynitrogen anions in tantalum–nitrogen compounds at high pressure. *Angew. Chem. Int. Ed.* **60**, 9003–9008 (2021).
35. Bykov, M. et al. High-pressure synthesis of a nitrogen-rich inclusion compound $ReN_8{\cdot}xN_2$ with conjugated polymeric nitrogen chains. *Angew. Chem. Int. Ed.* **57**, 9048–9053 (2018).
36. Bykov, M. et al. High-pressure synthesis of metal–inorganic frameworks $Hf_4N_{20}{\cdot}N_2$, $WN_8{\cdot}N_2$, and $Os_5N_{28}{\cdot}3N_2$ with polymeric nitrogen linkers. *Angew. Chem. Int. Ed.* **59**, 10321–10326 (2020).
37. Salke, N. P. et al. Tungsten hexanitride with single-bonded armchairlike hexazine structure at high pressure. *Phys. Rev. Lett.* **126**, 065702 (2021).
38. Wang, X., Li, J., Zhu, H., Chen, L. & Lin, H. Polymerization of nitrogen in cesium azide under modest pressure. *J. Chem. Phys.* **141**, 044717 (2014).
39. Peng, F., Yao, Y., Liu, H. & Ma, Y. Crystalline LiN_5 predicted from first-principles as a possible high-energy material. *J. Phys. Chem. Lett.* **6**, 2363–2366 (2015).
40. Shen, Y. et al. Novel lithium—nitrogen compounds at ambient and high pressures. *Sci. Rep.* **5**, 14204 (2015).
41. Steele, B. A. & Oleynik, I. I. Sodium pentazolate: a nitrogen rich high energy density material. *Chem. Phys. Lett.* **643**, 21–26 (2016).
42. Steele, B. A. & Oleynik, I. I. Novel potassium polynitrides at high pressures. *J. Phys. Chem. A* **121**, 8955–8961 (2017).
43. Xia, K. et al. Pressure-stabilized high-energy-density alkaline-earth-metal pentazolate salts. *J. Phys. Chem. C* **123**, 10205–10211 (2019).
44. Zhang, J., Zeng, Z., Lin, H.-Q. & Li, Y.-L. Pressure-induced planar N_6 rings in potassium azide. *Sci. Rep.* **4**, 4358 (2014).

45. Steele, B. A. et al. High-pressure synthesis of a pentazolate salt. *Chem. Mater.* **29**, 735–741 (2016).
46. Prasad, D. L. V. K., Ashcroft, N. W. & Hoffmann, R. Evolving structural diversity and metallicity in compressed lithium azide. *J. Phys. Chem. C* **117**, 20838–20846 (2013).
47. Li, J. et al. Pressure-induced polymerization of nitrogen in potassium azides. *EPL* https://doi.org/10.1209/0295-5075/104/16005 (2013).
48. Wang, X. et al. Polymerization of nitrogen in lithium azide. *J. Chem. Phys.* https://doi.org/10.1063/1.4826636 (2013).
49. Zhang, M., Yan, H., Wei, Q., Wang, H. & Wu, Z. Novel high-pressure phase with pseudo-benzene "N_6" molecule of LiN_3. *EPL* https://doi.org/10.1209/0295-5075/101/26004 (2013).
50. Zhang, M. et al. Structural and electronic properties of sodium azide at high pressure: a first principles study. *Solid State Commun.* **161**, 13–18 (2013).
51. Yu, H. et al. Polymerization of nitrogen in ammonium azide at high pressures. *J. Phys. Chem. C* **119**, 25268–25272 (2015).
52. Zhang, M., Yan, H., Wei, Q. & Liu, H. A new high-pressure polymeric nitrogen phase in potassium azide. *RSC Adv.* **5**, 11825–11830 (2015).
53. Laniel, D., Weck, G., Gaiffe, G., Garbarino, G. & Loubeyre, P. High-pressure synthesized lithium pentazolate compound metastable under ambient conditions. *J. Phys. Chem. Lett.* **9**, 1600–1604 (2018).
54. Laniel, D., Weck, G. & Loubeyre, P. Direct reaction of nitrogen and lithium up to 75 GPa: synthesis of the Li_3N, LiN, LiN_2, and LiN_5 compounds. *Inorg. Chem.* **57**, 10685–10693 (2018).
55. Bykov, M. et al. Stabilization of pentazolate anions in the high-pressure compounds Na_2N_5 and NaN_5 and in the sodium pentazolate framework $NaN_5{\cdot}N_2$. *Dalton Trans.* **50**, 7229–7237 (2021).
56. Eremets, M. I. et al. Polymerization of nitrogen in sodium azide. *J. Chem. Phys.* **120**, 10618–10623 (2004).
57. Medvedev, S. A. et al. Phase stability of lithium azide at pressures up to 60 GPa. *J. Phys. Condens. Matter* https://doi.org/10.1088/0953-8984/21/19/195404 (2009).
58. Zhu, H. et al. Pressure-induced series of phase transitions in sodium azide. *J. Appl. Phys.* https://doi.org/10.1063/1.4776235 (2013).
59. Ji, C. et al. Pressure-induced phase transition in potassium azide up to 55 GPa. *J. Appl. Phys.* **111**, 112613 (2012).
60. Ji, C. et al. High pressure X-ray diffraction study of potassium azide. *J. Phys. Chem. Solids* **72**, 736–739 (2011).
61. Holtgrewe, N., Lobanov, S. S., Mahmood, M. F. & Goncharov, A. F. Photochemistry within compressed sodium azide. *J. Phys. Chem. C* **120**, 28176–28185 (2016).
62. Bykov, M. et al. Dinitrogen as a universal electron acceptor in solid-state chemistry: an example of uncommon metallic compounds $Na_3(N_2)_4$ and NaN_2. *Inorg. Chem.* **59**, 14819–14826 (2020).
63. Hou, D. et al. Phase transition and structure of silver azide at high pressure. *J. Appl. Phys.* **110**, 023524 (2011).
64. Tomasino, D., Kim, M., Smith, J. & Yoo, C.-S. Pressure-induced symmetry-lowering transition in dense nitrogen to layered polymeric nitrogen (LP-N) with colossal Raman intensity. *Phys. Rev. Lett.* **113**, 205502 (2014).
65. Olijnyk, H. High pressure X-ray diffraction studies on solid N_2 up to 43.9 GPa. *J. Chem. Phys.* **93**, 8968–8972 (1990).

Methods

DAC experiments. The high-pressure, high-temperature behaviour of KN_3 was studied on two samples intended for combined XRD/Raman measurements and another four samples for Raman measurements. BX90-type DACs[66], equipped with Boehler–Almax-type seats and conical diamond anvils[67], and symmetric-type DACs, with standard-design seats and diamond anvils (Almax, EasyLab), were used for single-crystal/powder diffraction and Raman measurements, respectively. A powder sample of potassium azide KN_3 was placed in sample chambers of DAC equipped with diamond anvils with the culets of 100–300 μm in diameter for single-crystal and powder-diffraction XRD and Raman experiments. Rhenium foil preindented to a thickness of 30 μm served as a gasket. Ruby chips were placed inside the sample chambers for pressure measurement.

The XRD sample had no pressure-transmitting medium. All of the Raman samples were loaded with nitrogen gas at a high pressure of 0.15 GPa at room temperature. Raman samples 1 and 2 were quenched to below 2 GPa at room temperature while samples 3 and 4 were quenched to below 3 GPa at liquid-nitrogen temperature using a continuous flow He/N_2 cryostat. All samples were compressed up to the target pressures and laser-heated ($\lambda = 1064$ nm) using double-sided laser-heating systems of the GSECARS (APS, Argonne) or ISSP (Hefei) beamlines (see below). Laser heating of KN_3 in the DAC was performed without any absorber by directly coupling near infrared laser radiation with the sample. KN_3 is a weak absorber at 50–60 GPa; however, it can be coupled to the laser via grain boundaries and other defects, although care must be taken as it tends to run away once the temperature becomes higher than approximately 1000 K. Thus the temperature at which the reported below reactivity is reported should be considered cautiously. The heated area becomes non-transparent; we performed XRD and Raman mapping of these areas where available.

X-Ray diffraction measurements were performed at the GSECARS beamline (13IDD, APS, Argonne). We used monochromatic X-ray beam ($\lambda = 0.2952$ Å) focused down to $3 \times 3\,\mu m^2$ by a Kirkpatrick–Baez mirror system and diffraction patterns were collected on a Pilatus 1M detector (CdTe). For the single-crystal XRD measurements, samples were rotated around a vertical ω-axis within a ±35° range. The diffraction images were collected with an angular step $\Delta\omega = 0.5°$ and an exposure time of 1 s or 2 s per frame. Please see below for details on the single-crystal X-ray diffraction analysis and structural solution.

Raman spectra of the sample studied at GSECARS using XRD combined with laser heating were measured concomitantly using the GSECARS Raman system with the excitation wavelength of 532 nm in the spectral range of 10 to 4000 cm^{-1} with a 4 cm^{-1} spectral resolution (see below). The Raman spectra of the laser heated at ISSP samples were examined with 532 and 660 nm excitation lines using a similar custom system coupled to a continuous flow cryostat (see below).

Laser heating and cryogenic cooling systems. The double-sided laser-heating systems of GSECARS (APS, Sector 13, Argonne)[68] features the flat top focal spot of 10 μm in diameter. The sample temperature was measured radiometrically (grey body approximation). The thermal radiation was recorded with a Princeton grating spectrometer (300 mm focal length) combined with PIXIS and PiMAx charge-coupled device array detectors.

The double-sided laser heating system at ISSP (Hefei) is combined with the Raman confocal system thus making concomitant Raman probing of the heating area very convenient[69]. Another similar Raman system coupled to a continuous flow He/N_2 cryostat was used for Raman experiment, where the sample was investigated following unloading at room and low (78 K) temperatures[70].

Raman systems. The full description of the confocal GSECARS Raman systems, which has been used concomitantly to XRD measurements, has been published elsewhere[71]. It features five excitation laser lines from the ultraviolet to near-infrared, which can be automatically changed and double-sided laser heating.

Two Raman systems at ISSP (Hefei) are described in the previous sections.

Single-crystal XRD analysis. We used the CrysAlis^{Pro} software package for the analysis of the single-crystal diffraction data (indexing, data integration, frame scaling and absorption correction). To calibrate an instrumental model in the CrysAlis^{Pro} software, that is, the sample-to-detector distance, detector's origin, offsets of goniometer angles, and rotation of both X-ray beam and the detector around the instrument axis, we used a single crystal of orthoenstatite ($(Mg_{1.93}Fe_{0.06})(Si_{1.93}, Al_{0.06})O_6$, *Pbca* space group, $a = 8.8117(2)$, $b = 5.18320(10)$ and $c = 18.2391(3)$ Å). Using the Olex2 crystallography software package, the structures were solved with the SHELXT structure solution program[72] using Intrinsic Phasing and refined with the SHELXL[73] refinement package using least-squares minimization. The powder diffraction images were integrated to powder patterns with Dioptas software[74]. Le-Bail fits of the diffraction patterns were performed with the Jana2006 software[75]. A- and B-level alerts of the IUCR's CheckCIF routine are related to data incompleteness, which is unavoidable in a high-pressure diffraction experiment.

Structural analysis of cold-compressed KN_3. Most of the cold-compressed KN_3 sample produces weak powder diffraction pattern, as shown in Supplementary Fig 2; however, we were able to locate the grain that produces the poor-quality single-crystal diffraction pattern. The diffraction patterns collected at the positions of the powder-like and single-crystal samples demonstrate that the same phase is present in both collection spots. The peak positions are only slightly different, which can be explained by pressure gradients in the sample without a pressure-transmitting medium. The differences in the distribution of intensities are clearly related to the strong preferred orientation of the single-crystal sample.

The unconstrained lattice determination from the single-crystal XRD dataset reveals the *I*-centred lattice with $a = 5.425(13)$, $b = 5.487(11)$, $c = 4.67(4)$ Å, $\alpha = 90.6(4)°$, $\beta = 92.2(4)°$, $\gamma = 90.22(17)°$. These parameters are close to the parameters expected for the *I*4/*mcm* KN_3 compressed to ~50 GPa; however, the structure is clearly distorted. The refinement of the *I*4/*mcm* KN_3 structure using our single-crystal dataset resulted in the good agreement factor $R_1 = 11.03\%$ for 32/5 data to parameter ratio. This agreement demonstrates that we indeed deal with the distorted *I*4/*mcm* structure rather than with a completely different structure type, like predicted *C*2/*m* KN_3. The unconstrained lattice refinement suggests either monoclinic or triclinic symmetry. By a group–subgroup transformation we have generated the *I*2/*c* model of KN_3 from the high-symmetry *I*4/*mcm*. The refinement converged with a slightly worse $R_1 = 13.73\%$ at a 56/8 data/parameter ratio. Although this value is higher than for the *I*4/*mcm* model, the use of monoclinic symmetry is justified by the lattice metrics. We provide the structure model of *I*2/*c* KN_3 below (Supplementary Table 1) with a notice that the quality of the dataset allows to distinguish main structural motifs, while it should not be used for the judgement about specific structure details. For example, although the refined N–N distances in the azide group are reasonable (1.17(1) Å) they should be used with caution when considered in systematic comparison with other azides at similar conditions. Similarly, further symmetry reduction to triclinic does not provide additional reliable structural information.

Theoretical calculations. First-principles calculations were conducted using the Vienna ab initio simulation package (VASP)[76]. The structure was optimized using the Perdew–Burke–Ernzerhof functional within the generalized gradient approximation[77]. The cutoff energy of plane waves was set to 600 eV. The partition of the first Brillouin zone into a grid of k-points was carried out with a resolution $2\pi \times 0.03$ Å^{-1}. To calculate the phonon dispersions and Raman-active vibration modes of Γ point the PHONOPY program was employed with VASP interfaces[78]. The electronic density of state and band structure were calculated at a resolution $2\pi \times 0.015$ Å^{-1}. Electron dispersion curves and density of states were plotted using the SUMO software[79].

The crystal structures of *I*4/*mcm*-KN_3, *C*2/*m*-KN_3 and *P*6/*mmm*-KN_3 were relaxed at 30 and 50 GPa. Using the relaxed structures, we constructed likely transition paths (20 for each transition) and optimized each of them, which allowed us to find the lowest energy path for each transition. At the first stage, the most convenient representations of the initial and final structures are sought; it allows one to determine the optimal representation of unit cells of these structures[80,81]. At this stage, two unit cells are transformed to have the same number of atoms taking into account the total symmetry of non-equivalent supercells whose number is determined within the Hart–Forcade theory[82]. For each of two structures, we work only with lattices and seek such unit cell settings (among all possible choices of the unit cell) that are closest to each other. At the second stage, atoms are placed back into two generated supercells and the algorithm finds such correspondence, or mapping, between the two structures such that the total distance travelled by all of the atoms, from the initial to the final structure, is minimal[80,81]. It is important to note that the mapping algorithm is not commutative; thus, for each pair of structures, the algorithm produced the ten likeliest A → B and B → A paths, respectively). The above-mentioned initial paths of phase transitions were optimized using the variable-cell nudged-elastic-band method[83] as implemented in USPEX[84–86]. Each path consisted of 20 intermediate structures (images). The *I*4/*mcm*-KN_3 has 16 atoms in the unit cell, whereas *C*2/*m*-KN_3 and *P*6/*mmm*-KN_3 have eight atoms. According to the mapping algorithm, two end structures must be extended to the cell with an equal number of atoms. Thus, the transitions from *I*4/*mcm*-KN_3 to *C*2/*m*-KN_3 at 30 GPa and from *I*4/*mcm*-KN_3 to *P*6/*mmm*-KN_3 at 50 GPa were simulated in cells with 16 atoms. The transition from *C*2/*m*-KN_3 to *P*6/*mmm*-KN_3 at 50 GPa was simulated in cells with eight atoms. For accurate determination of transition states and intermediate minima corresponding to metastable transition states, we used the climbing image–descending image technique[87]. The spring constants for the variable-cell nudged-elastic-band method were varied from 3 to 6 eV Å^{-2}. The halting criterion for the calculation was set as root mean square forces on images that are less than 0.003 eV Å^{-1}. All calculations were based on density functional theory[88,89] within the generalized gradient approximation (PBE functional)[77], and the projector augmented wave method[90,91] as implemented in the VASP[76,92,93] package. The plane–wave energy cutoff of 600 eV was used, ensuring excellent convergence of total energies, forces and stresses. Crystal structures were relaxed until the maximum net force on atoms became less than 0.01 eV Å^{-1}. The Monkhorst–Pack scheme[94] was used to sample the Brillouin zone, using 8 × 8 × 8 k-points mesh for all KN_3 phases.

Data availability

The datasets generated during and/or analysed during the current study are available at https://doi.org/10.6084/m9.figshare.19236573 (ref. [95]),

https://doi.org/10.6084/m9.figshare.19236609 (ref. [96]) and https://doi.org/10.6084/m9.figshare.19228086.v1 (ref. [97]). CSD 2022907 and 2094084 contain crystallographic data for the $K_3(N_2)_4$ and K_2N_6 structures. These data can be obtained free of charge from FIZ Karlsruhe at www.ccdc.cam.ac.uk/structures. Source Data are provided with this paper.

References

66. Kantor, I. et al. BX90: a new diamond anvil cell design for X-ray diffraction and optical measurements. *Rev. Sci. Instrum.* **83**, 125102 (2012).
67. Boehler, R. New diamond cell for single-crystal X-ray diffraction. *Rev. Sci. Instrum.* **77**, 115103 (2006).
68. Prakapenka, V. B. et al. Advanced flat top laser heating system for high pressure research at GSECARS: application to the melting behavior of germanium. *High Pressure Res.* **28**, 225–235 (2008).
69. Cheng, P. et al. Polymorphism of polymeric nitrogen at high pressures. *J. Chem. Phys.* **152**, 244502 (2020).
70. Goncharov, A. F. et al. Backbone NxH compounds at high pressures. *J. Chem. Phys.* https://doi.org/10.1063/1.4922051 (2015).
71. Holtgrewe, N., Greenberg, E., Prescher, C., Prakapenka, V. B. & Goncharov, A. F. Advanced integrated optical spectroscopy system for diamond anvil cell studies at GSECARS. *High Pressure Res.* **39**, 457–470 (2019).
72. Sheldrick, G. M. SHELXT— integrated space-group and crystal-structure determination. *Acta Crystallogr. A* **71**, 3–8 (2015).
73. Sheldrick, G. Crystal structure refinement with SHELXL. *Acta Crystallogr. C* **71**, 3–8 (2015).
74. Prescher, C. & Prakapenka, V. B. DIOPTAS: a program for reduction of two-dimensional X-ray diffraction data and data exploration. *High Pressure Res.* **35**, 223–230 (2015).
75. Václav, P., Michal, D. & Lukáš, P. Crystallographic computing system JANA2006: general features. *Zeit. Kristallogr.* **229**, 345–352 (2014).
76. Kresse, G. & Furthmuller, J. Efficient iterative schemes for ab initio total-energy calculations using a plane-wave basis set. *Phys. Rev. B* **54**, 11169–11186 (1996).
77. Perdew, J. P., Burke, K. & Ernzerhof, M. Generalized gradient approximation made simple. *Phys. Rev. Lett.* **77**, 3865–3868 (1996).
78. Togo, A. & Tanaka, I. First principles phonon calculations in materials science. *Scr. Mater.* **108**, 1 (2015).
79. Ganose, A. M., Jackson, A. J. & Scanlton, D. O. SUMO: command-line tools for plotting and analysis of periodic ab initio calculations. *J. Open Source Softw.* **3**, 717 (2018).
80. Therrien, F., Graf, P. & Stevanović, V. Matching crystal structures atom-to-atom. *J. Chem. Phys.* **152**, 074106 (2020).
81. Stevanović, V. et al. Predicting kinetics of polymorphic transformations from structure mapping and coordination analysis. *Phys. Rev. Mater.* **2**, 033802 (2018).
82. Hart, G. L. W. & Forcade, R. W. Algorithm for generating derivative structures. *Phys. Rev. B* **77**, 224115 (2008).
83. Qian, G.-R. et al. Variable cell nudged elastic band method for studying solid–solid structural phase transitions. *Comput. Phys. Commun.* **184**, 2111–2118 (2013).
84. Oganov, A. R. & Glass, C. W. Crystal structure prediction using ab initio evolutionary techniques: principles and applications. *J. Chem. Phys.* https://doi.org/10.1063/1.2210932 (2006).
85. Oganov, A. R., Lyakhov, A. O. & Valle, M. How evolutionary crystal structure prediction works—and why. *Acc. Chem. Res.* **44**, 227–237 (2011).
86. Oganov, A. R., Ma, Y., Lyakhov, A. O., Valle, M. & Gatti, C. Evolutionary crystal structure prediction as a method for the discovery of minerals and materials. *Rev. Mineralogy Geochem.* **71**, 271–298 (2010).
87. Henkelman, G., Uberuaga, B. P. & Jónsson, H. A climbing image nudged elastic band method for finding saddle points and minimum energy paths. *J. Chem. Phys.* **113**, 9901–9904 (2000).
88. Hohenberg, P. & Kohn, W. Inhomogeneous electron gas. *Phys. Rev.* **136**, B864–B871 (1964).
89. Kohn, W. & Sham, L. J. Self-consistent equations including exchange and correlation effects. *Phys. Rev.* **140**, A1133–A1138 (1965).
90. Blöchl, P. E. Projector augmented-wave method. *Phys. Rev. B* **50**, 17953 (1994).
91. Kresse, G. & Joubert, D. From ultrasoft pseudopotentials to the projector augmented-wave method. *Phys. Rev. B* **59**, 1758–1775 (1999).
92. Kresse, G. & Hafner, J. Ab initio molecular dynamics for liquid metals. *Phys. Rev. B* **47**, 558–561 (1993).
93. Kresse, G. & Hafner, J. Ab initio molecular-dynamics simulation of the liquid-metal–amorphous-semiconductor transition in germanium. *Phys. Rev. B* **49**, 14251–14269 (1994).
94. Monkhorst, H. J. & Pack, J. D. Special points for Brillouin-zone integrations. *Phys. Rev. B* **13**, 5188–5192 (1976).
95. Samtsevich, A. *Details of Theoretical Calculations of the Transition Pathways Between the Candidate Structures* (FigShare, 2022); https://doi.org/10.6084/m9.figshare.19236573
96. Chepkasov, I. *Details of Theoretical Calculations of the Electronic and Phonon Band Structure of Novel High-Pressure K_2N_6* (FigShare, 2022); https://doi.org/10.6084/m9.figshare.19236609
97. Bykov, M. Synchrotron Dataset of laser-heated KN3 at ~50 GPa (FigShare, 2022); https://doi.org/10.6084/m9.figshare.19228086.v1

Acknowledgements

This work at ISSP was supported by the National Natural Science Foundation of China (grant nos. 11504382, 21473211, 11674330, 51672279, 11874361, 11774354 and 51727806), the CASHIPS Director's Fund (grant no. YZJJ201705), the Chinese Academy of Science (grant nos. YZ201524 and YZJJ2020QN22) and a Science Challenge Project (no. TZ201601). This research at Carnegie and APS was sponsored by the Army Research Office and was accomplished under the Cooperative Agreement Number W911NF-19-2-0172. A.R.O., I.C. and A.I.S acknowledge funding from Russian Science Foundation (grant no. 19-72-30043). GeoSoilEnviroCARS (The University of Chicago, Sector 13), Advanced Photon Source (APS), Argonne National Laboratory is supported by the National Science Foundation—Earth Sciences (EAR-1634415). Use of the GSECARS Raman System was supported by the NSF MRI Proposal (EAR-1531583). The Advanced Photon Source is a US Department of Energy (DOE) Office of Science User Facility operated for the DOE Office of Science by Argonne National Laboratory under contract no. DE-AC02-06CH11357. The theoretical calculations were performed using Arkuda and Oleg supercomputer of Skoltech.

Author contributions

Y.W., M.B. and A.F.G. conceived the research and designed the experiments. Y.W., M.B., X.Z., E.G., S.C., V.B.P. and S.-q.J performed the experiment. E.B., Y.W., M.B. and A.F.G. analysed the data. I.C., A.S. and A.R.O. performed and analysed the calculations. A.F.G., Y.W., M.B. and A.S. wrote the manuscript. All authors reviewed and discussed the manuscript during preparation.

Competing interests

The authors declare no competing interests.

Additional information

Supplementary information The online version contains supplementary material available at https://doi.org/10.1038/s41557-022-00925-0.

Correspondence and requests for materials should be addressed to Alexander F. Goncharov.

Peer review information *Nature Chemistry* thanks Karl Christe, Thomas Klapötke and the other, anonymous, reviewer(s) for their contribution to the peer review of this work.